Sensors and Actuators A 264 (2017) 289–297

Contents lists available at ScienceDirect

Sensors and Actuators A: Physical

journal homepage: www.elsevier.com/locate/sna

# Bioinspired flexible microfluidic shear force sensor skin

Jianzhu Yin[a], Veronica J. Santos[b], Jonathan D. Posner[a,c,d,*]

[a] Mechanical Engineering, University of Washington, Seattle, WA, USA
[b] Mechanical and Aerospace Engineering, University of California, Los Angeles, CA, USA
[c] Chemical Engineering, University of Washington, Seattle, WA, 98195, USA
[d] Family Medicine, University of Washington, Seattle, WA, 98195, USA

ARTICLE INFO

*Article history:*
Received 21 March 2017
Received in revised form 19 July 2017
Accepted 1 August 2017
Available online 8 August 2017

*Keywords:*
Resistive sensor
Conductive fluid
Flexible sensor
Microfluidic shear force sensor
Sensor skin
Soft lithography

ABSTRACT

There is a need to gather rich, real-time tactile information to enhance robotic hand performance during haptic exploration and object manipulation. Measuring shear forces is useful for grasping and manipulating objects; however, there are limited effective shear sensing strategies that are compatible with existing end effectors. Here, we report a bioinspired and flexible, resistive microfluidic shear force sensor skin. The sensor skin is wrapped around a finger-shaped end effector and fixed at the location of the nail bed. When the skin is subjected to shear force, one side of the skin experiences tension while the other side experiences compression and bulges similar to a human fingerpad. The tension and compression are measured by liquid metal strain gauges, embedded in PDMS, that are strategically placed adjacent to the nail bed, away from regions of direct finger-object contact. We present the sensor design, a finite element analysis static mechanical characterization model, as well as static response experiments. The resistive shear sensing skin exhibits greater than 10-bit dynamic range (up to 5 N) that is insensitive to the applied normal force. The resistive shear sensing skin is intrinsically flexible and immune to fatigue and other problems of solid-state sensors when subjected to repeated, large strains.



## 1. Introduction

Human fingertips are equipped with mechanoreceptors to collect tactile information so that we can precisely control muscle coordination during tasks such as haptic exploration and object manipulation [1]. This information enables humans to deduce some object properties that cannot be inferred from other modes of sensing, such as vision [2]. Despite the importance of tactile sensing, it is not widely implemented in robot hands or prostheses [3]. A robot hand equipped with a deformable multimodal tactile sensor has been used to demonstrate the ability to perceive local shape, which could be used to advance robot autonomy and provide haptic feedback to human teleoperators [4].

Haptic exploration and object manipulation benefit from rich, real-time tactile feedback through physical contact [3,5–7]. It has been shown that human operators tend to exert more gripping force than needed when using visual feedback alone [2]. Damage of the manipulated object and/or the end effector itself due to overloading is also of concern when tactile feedback is not available [8]. Restoring the sense of touch may be valuable in delicate and precise manipulation applications such as tele-operation of minimally invasive surgery [5]. Several tactile sensors and algorithms have been developed to pick up objects of varying mass and texture [9], estimate the contents of a container [10], and distinguish light and firm touch [11].

Spatially and temporally resolved normal and shear stresses are critical mechanical measurements that need to be resolved on artificial fingertips. Sensor design criteria are typically task-specific; however, general sensor specifications can be guided by physiological properties of human mechanoreceptors [6,12]. Within the scope of in-hand manipulation, normal and shear forces up to 10 N should be resolved with an optimal dynamic range of 1000 [6]. In practice, sensing ranges of 0.3–50 N have been demonstrated in engineered tactile sensors according to their target application [3,5,13,14]. A normal force spatial resolution of 1.25 mm has been suggested to properly resolve object geometric features [3,6,15]. Kyung et al. have shown that humans have high normal force spatial resolution for interactions below 32 Hz [16]. It is less clear how well shear forces need to be spatially resolved, spurring further research of desired resolution during in-hand manipulation. Low latency temporal response contributes to better control stability, faster reflex-like responses, and can enable inference of surface properties such as roughness, shape, or coefficient of friction during

* Corresponding author at: University of Washington, Mechanical Engineering Building, Stevens Way, Box 352600, Seattle, WA 98195, USA.
*E-mail address:* jposner@uw.edu (J.D. Posner).

http://dx.doi.org/10.1016/j.sna.2017.08.001
0924-4247/

haptic exploratory motion [17–21]. Humans can detect vibrations as high as 700 Hz although frequencies such as 100 Hz, 250 Hz or 1000 Hz have been proposed for vibration sensors for specific applications [3,6,13–15].

A wide variety of tactile sensors have been demonstrated including whole finger [22] and artificial skin based sensors that are compatible with existing robotic and prosthetic hand actuators [23–36]. Sensor skins that can be wrapped conformally around robotic manipulators minimize the need for modification of the end effector. Skin based sensors have been fabricated with liquid-metal-based transducers embedded in elastomers. Polydimethylsiloxane (PDMS) based sensors have been demonstrated as robust, non-toxic, highly flexible, low cost, and easily fabricated [23,28–30], [34,36–39]. Liquid metal filled channels, such as those filled with eutectic gallium indium alloy (eGaIn), are intrinsically immune to cracks and fatigue, suitable for conformal wrapping and large, repetitive strains [37,40–43]. eGaIn is a conductive liquid metal at room temperature and can form microstructures with a 2 μm spatial resolution by injection into micro-channels [23,39,40,44–47]. eGaIn traces that are 200–300 μm wide can be rapidly patterned by microcontact printing, 3D printing, or stencil lithography [48–51].

A variety of miniaturized microelectromechanical system soft sensor skins with liquid metal that use capacitive, resistive and inductive sensing modalities have been developed [23,38,39,44,45,47]. Capacitive sensors are typically composed of two flat-plate electrodes separated by a dielectric material and benefit from high sensitivity, ease of array fabrication, and high spatial resolution [23], [36,44]. We previously developed a light touch microfluidic normal force sensor that achieved a spatial resolution of 1 mm with a 5 by 5 array of deformable parallel plate capacitors and was calibrated from 0 to 2.5 N [23]. Roberts et al. presented a soft sensor that used differential measurements in multiple parallel plate capacitor taxels to detect shear deformation in two orthogonal dimensions [44]. Capacitive based sensors are susceptible to electromagnetic interference, crosstalk, and parasitic capacitance.

Resistive sensors, including strain gauges and piezoresistive sensors, convert deformation to change of resistance, which can be easily measured by 4-wire sensing or a Wheatstone bridge circuit. Resistive sensors generally have good sensitivity over a large sensing range, high scanning rate, and are easy to design and implement. Their weaknesses include lower repeatability, high power consumption, and sensitivity to temperature. Park et al. presented an artificial skin capable of measuring uniaxial strain in three directions constructed with serpentine and spiral eGaIn channels; however, the minimal normal force that could be sensed was 7.4 N [47]. Majidi et al. developed a single microfluidic channel resistive sensor skin that measures curvature and could be useful in applications such as angular position feedback of an articulated joint [46].

There are only a few strategies to measure shear force, such as pairs of planar strain gauges [27], vertical cantilevers [49], or clusters of normal force taxels that are strategically positioned in pairs or quadruples such that shear force acting at the center of the sensor cluster results in combinations of normal force readings [36,40,41,50]. Sensor sensitivity can be enhanced by adding a bump or ridge on the sensing surface or adding rigid force-posts embedded in the media over the sensing elements [40,41,50], although this approach suffers from reduced spatial resolution since it takes several taxels to construct a single sensing unit. Using a combination of normal force sensors could falsely generate shear force readings from normal forces that are non-uniform or localized on an individual taxel. Previous reports on shear force sensors collectively demonstrate calibration under a single normal force level and rarely discuss the influence of pre-applied normal force. Shear sensors typically measure forces at the point of physical contact between the sensor and object, but, in robotic applications, the location of contact may be arbitrary and would necessitate a large number of distributed sensors. Tactile sensors that resolve shear forces away from the point of contact may be advantageous, especially when faced with constraints on space, such as the small region of a fingerpad. Sensing modalities that do not require localized sensing for direct measurement of stimuli can be displaced to make room for other sensing modalities, such as normal force.

In this paper, we develop a bioinspired, thin and flexible liquid metal filled resistive PDMS microchannel shear force sensing skin. The sensor skin is wrapped around a finger-shaped effector and fixed at the location of the nail bed. When the skin is subjected to shear force it results in one side of the skin in tension and the other side in compression that buckles and bulges similar to a human fingertip. The tension and compression are measured by embedded liquid metal strain gauges that are strategically placed adjacent to the nail bed, away from the point of finger-object contact. We present the sensor design, a finite element analysis (FEA) static mechanical characterization model in addition to an analytical approach, as well as static response experiments. We show that the resistive shear sensing skin exhibits large dynamic range that is insensitive to the applied normal force over a range of shear forces. The resistive shear sensing skin is intrinsically flexible and immune to fatigue when subjected to repeated large strains.

## 2. Sensor design and theory of operation

The shear sensing skin design is inspired by the layered structure of the human fingertip. Skin consists of epidermis (outermost layer), dermis, and subcutaneous fat tissue. While all of these layers are soft relative to the underlying bone, the subcutaneous fat tissue is much softer than epidermis and dermis, thus, skin tends to shear and slide with respect to the underlying bone when shear force is applied to the finger pad. This deformation results in tension on one side of the fingerpad and compression on the other side. We can resolve shear force by leveraging the asymmetry in the strain that occurs across the fingerpad, provided there is little to no Poisson's effect at the shear sensing taxels. The Poisson's effect is negligible when normal forces are not applied directly to the shear force sensing taxels.

Fig. 1 shows a schematic of the resistive shear sensing skin and mode of operation. The sensor skin wraps around a rigid artificial fingertip and is fixed with two mounting brackets on the radial and ulnar aspects near the perimeter of a human finger nail bed, as shown in Fig. 1A. The eGaIn-filled microchannel strain gauges are embedded in the skin, adjacent to the fixed mounting brackets. The interface between the rigid fingertip and flexible skin is lubricated so that the skin can slide easily relative to the fingertip. The skin slides relative to the rigid finger, when subject to a radioulnar shear force, putting the opposing sides of the sensor skin in compression (buckling) and tension (Fig. 1B). The measured asymmetric strains across the pair of gauges are used to determine the shear force applied on the fingerpad in the radioulnar direction. The shear force sensor is insensitive to shear force in $z$-direction because both gauges will experience the same strain due to the symmetry of the system with respect to $z$-direction. The long strips in the gauge are aligned with the principal direction of circumferential strain, with the goal of maximizing sensitivity to shear forces. The gauge placement is designed to be insensitive to the normal force applied at the point of contact. This shear sensing skin design may be compatible with a range of artificial fingertip geometries, when appropriately calibrated to address variations in finger surface geometry as well as friction between the sensor skin and the end effector.

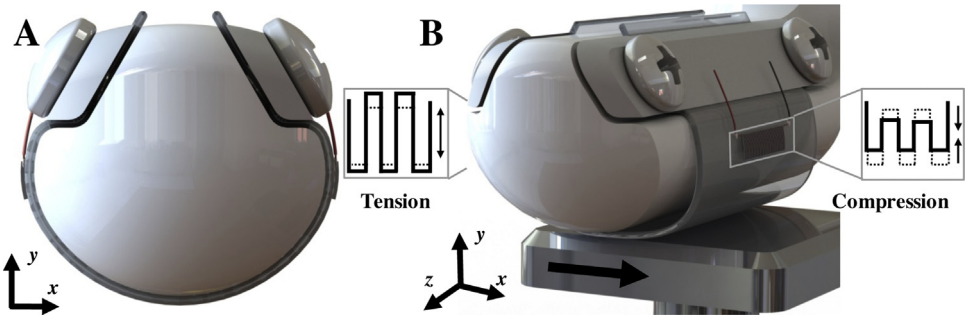


**Fig. 1.** Schematics of the resistive shear sensing skin design and theory of operation. (A) The artificial skin is conformally wrapped around a rigid fingertip and affixed using mounting brackets that mimic the region of nail bed attachment on a human finger. The eGaIn-filled microchannel strain gauges are located on the radial and ulnar aspects of the finger. (B) A rigid plate applies a shear stress that drives the skin to slide relative to the rigid finger and results in the opposing sides of the sensor skin to compress (buckle) and stretch. The difference in resistance between the two opposing strain gauges is used to measure the shear applied shear force.

The strain gauge sensor microchannel design is a compromise between signal to noise ratio, power consumption, and microfabrication constraints. Considering $N$ strips each of length $L$ forming a strain gauge with total width $W$, the total length of the conductor consists of $NL$ in the longitudinal direction and $W$ in the transverse direction. Since $N \gg 1$, the transverse part can be ignored and the total resistance is approximately $\rho NL/(wh)$ where $\rho$ is resistivity of the liquid filling the channel and $w$ and $h$ are the respective width and height of the microchannel. When the skin deforms under shear stress the channels with length $L$ are either elongated or compressed resulting in a proportional change in resistance. The measured resistance change can be related to strain using the gauge factor $F = \frac{\Delta R}{R_0}/\varepsilon$, where $\Delta R$ is the change of resistance, $R_0$ is the resistance at the un-deformed state, and $\varepsilon$is the strain. A uniaxial tensile stress with linear elasticity at small strain yields, $\frac{\Delta R}{R_0} = \frac{1+\varepsilon}{(1-\upsilon\varepsilon)^2} - 1 \approx (1+2\upsilon)\varepsilon$ where $\upsilon$ is Poisson's ratio of the material. The Poisson's ratio of an incompressible elastomer is 0.5 resulting in an estimated gauge factor of $(1+2\upsilon) = 2$.

The power consumption of the strain gauge is $V^2/R = V^2 wh/\rho NL$ where $V$ is the applied voltage. These equations show that it is advantageous to maximize the sensor resistance because it minimizes the sensor power consumption and results in greater measured sensor response. Large sensor resistance can be achieved with small channel cross-section dimensions; however, there is a practical limit to the minimum channel cross-section dimensions because larger filling pressures and better sealing techniques are required to fill the channels with liquid metal as microchannel dimensions become smaller. In this work, we compromise these design constraints with 50 μm width and height and an approximately 210 mm long serpentine channel made of $N = 70$ strips that are $L = 3$ mm long. The calculated nominal resistance of each strain gauge is approximately 25 Ω, which is verified later in experiments described in Section 3.3.

## 3. Computational and experimental methodology

### 3.1. Numerical simulations of shear sensor

We developed steady, two-dimensional finite element solid mechanics models (COMSOL Multiphysics, Boston, MA) with linear elasticity to predict the sensor response to various normal and shear force loading conditions. We used these models to determine the appropriate placement of the strain gauges to obtain linear, high sensitivity sensor response that is independent of the applied normal force. The model was composed of two domains: one for the rigid fingertip core and one for the PDMS artificial skin. Young's modulus and Poisson's ratio of the fingertip were set to be 3.2 GPa and 0.3, respectively, in order to represent a rigid plastic material such as acrylic. We assumed the PDMS skin was a uniformly linear elastic and incompressible with a Young's modulus of 1.292 MPa, a Poisson's ratio of 0.5 (0.49 to avoid numerical instabilities). The mechanical properties of the PDMS were obtained through tensile tests described in the supplemental information. Linear elasticity was used to describe the stress-strain relation at the strain levels considered in the model. Throughout the modelling study, the maximum strain level was 9% and the true stress deviated from the linear estimation by less than 5.5%. While a hyperelastic model, such as Mooney-Rivlin, would be more accurate for describing strain softening at high loads, linear elasticity at lower loads is sufficient to validate the design and provide general guidelines for selecting sensor parameters such as spatial location, gauge size, channel dimension, etc.

We assumed that the strain gauges would not alter the PDMS material stiffness. The boundaries where the artificial skin was fastened to the fingernail were specified as fixed. The boundaries between the rigid fingertip and flexible PDMS skin were designated as non-penetrable contact. The skin can slide relative to the fingertip once friction, with a static Coulomb friction coefficient of 0.04, has been overcome. The static friction coefficient was determined from experiments (see supplemental information). The forces are uniformly distributed on a 5° arc at the bottom, center edge of the skin (the 0,−6.35 location in Fig. 3). The contact between the skin and stimulus (object contacting the fingertip) was not considered because, according to Saint-Venant's Principle, the sensor response is equivalent to that of a uniform boundary load at the contact location as long as the contact is sufficiently far from the sensor location. Since the friction force between the skin and rigid fingertip is path-dependent, the loads in both normal and shear direction in the model were applied in the same order as the experiments. The normal force was first applied and shear force increases from zero to the value of normal force in 0.1 N increments. Four cases were examined where normal forces were 0.5 N, 1 N, 1.5 N, and 2 N.

The rigid fingertip core was meshed with free triangular elements and the PDMS skin with mapped quadrilateral mesh elements. The maximum element size in the skin domain was set at 0.14 mm. The total number of elements was 1648 and minimum quality was 0.85 [52–54]. Further mesh refinement did not alter the results, suggesting that the mesh was sufficiently resolved. In post-processing, the strain in the circumferential direction was evaluated to strategically place the strain gauges in locations that yielded linear response, largest sensitivity, and independence to applied normal force on the palmar aspect of the fingertip. The normalized sensor response was defined as,

$$\tilde{\Delta R} = \frac{\Delta R_1}{R_{1,0}} - \frac{\Delta R_2}{R_{2,0}} = \mathrm{F}(\varepsilon_1 - \varepsilon_2) \quad (1)$$

where $F$ is the gauge factor, $R_{1,0}$ and $R_{2,0}$ are radial and ulnar strain gauge resistances when there is zero load, $\Delta R_1$ and $\Delta R_2$ are changes of resistances with respect to $R_{1,0}$ and $R_{2,0}$, respectively, and $\varepsilon_1$ and $\varepsilon_2$ are surface averaged tangential strain at the strain gauge locations, respectively. The normalized sensor response was calculated and plotted against shear force at different normal force levels.

### 3.2. Sensor fabrication

In this study, conventional soft lithography fabrication techniques were used to generate 50 μm microchannels and here we provide specific technical details relevant to our sensor fabrication [23]. The master for the serpentine channel was fabricated by first spin coating (PWM32, Headway Research, Garland, TX) SU-8 2025 photoresist (Microchem, Westborough, MA) at 1500 rpm onto a 4 in. silicon wafer. The wafer was soft baked by ramping up to 95 °C at 120 °C/hr for 7 mins and cooling to room temperature at 240 °C/hr. The master was exposed for 60 s in a broad wavelength aligner (AB-M, ABM, Scotts Valley, CA) whose intensity is 8.88 mW/cm$^2$ at 365 nm. Then the wafer was post baked by ramping to 95 °C at 300 °C/hr, for 7 mins and then cooled to room temperature at 300 °C/hr. The master was then developed for 6 mins and hard baked at 150 °C to improve mechanical stability. Trichloro(1H,1H,2H,2H-perfluorooctyl)silane (Sigma-Aldrich, St. Louis, MO) was evaporated onto the master in a desiccator to reduce the adhesion between PDMS and the mold. The thickness of the pattern on the master was measured to be 50 μm by a stylus profilometer (Alpha Step 200, KLA-Tencor, Milpitas, CA).

We used PDMS with a 10:1 elastomer to curing agent ratio (RTV 615, Momentive, Waterford, NY). Each half of the PDMS layer was fabricated using a two-step spin coating process by first spin coating at 500 rpm for 60 s, curing at 80 °C for 1 h in a desiccator under vacuum, and repeating to get a 0.3 mm thick layer. The patterned layer was peeled from the wafer and cut into desired shape of 47 mm by 20 mm with serpentine strain gauges that have a total sensor area of 7 mm by 3 mm. Reservoirs for each strain gauge were created by punching the patterned layer with a 710 μm cutting edge diameter, tin coated stainless steel puncher (CR0350255N20R4, SYNEO, Angleton, TX, USA). We bonded the patterned PDMS film to a flat piece of PDMS, fabricated by spin coating PDMS on a blank wafer, using 30 s of oxygen plasma treatment (PDC-001, Harrick Plasma, Ithaca, NY, USA) with a 500–600 mTorr pressure and RF power of 30 W. The patterned PDMS film was brought into contact with the flat PDMS film immediately after treatment and visual inspection for air entrapment. The assembly was elevated to 80 °C for 1 h to increase the bonding strength. We injected eGaIn (Gallium Indium Tin Eutectic, GalliumSource, LLC, Scotts Valley, CA, USA) into each strain gauge with a 22 gauge blunt needle (Weller KDS2212P, Apex Tool Group, Sparks, MD, USA). Two hundred fifty micron diameter copper wires (42978, Alfa Aesar, Ward Hill, MA, USA) were placed into each reservoir and sealed by dispensing uncured PDMS over the reservoirs and copper wires. The assembly was brought to 80 °C for 1 h in an oven to cure the PDMS that seals the reservoirs and adheres the copper wires to the PDMS film. Fig. 2 shows the fully assembled artificial skin embedded with eGaIn-filled microchannel strain gauges.

### 3.3. Characterization experimental setup, data acquisition, and post processing

We mounted the shear sensor on a three-dimensional linear stage to evaluate its performance under controlled normal and shear force loading, as shown in Fig. 3A. Three manual linear stages (433, Newport, Irvine, CA, USA) were assembled with right angle brackets (AP90, Thorlabs Inc., Newton, NJ, USA) to form three translational degrees of freedom, and were then fixed to an optical breadboard (PBH11105, Thorlabs Inc., Newton, NJ, USA). The stages were actuated manually with adjustment screws and Vernier micrometers (AJS100-2, SM-50, Newport, Irvine, CA, USA). A rotational stage (481-A, Newport, Irvine, CA, USA) was incorporated to enable fine-tuning of the direction of force loads and ensure that shear force loads were parallel to the fingertip surface tangent. Two acrylic plates were used to fasten the artificial skin to the radial and ulnar aspects of an artificial fingertip that was fabricated from an acrylic half-round with length of 20 mm and diameter of 12 mm. The fingertip was rigidly attached to the stage. The copper wires originating from the sensor reservoirs were soldered to 8 mm by 8 mm copper pads that were placed beside the plastic fingertip, adjacent to the sensor reservoirs. The copper pads provide stress relief for attachment to the external electronic equipment.

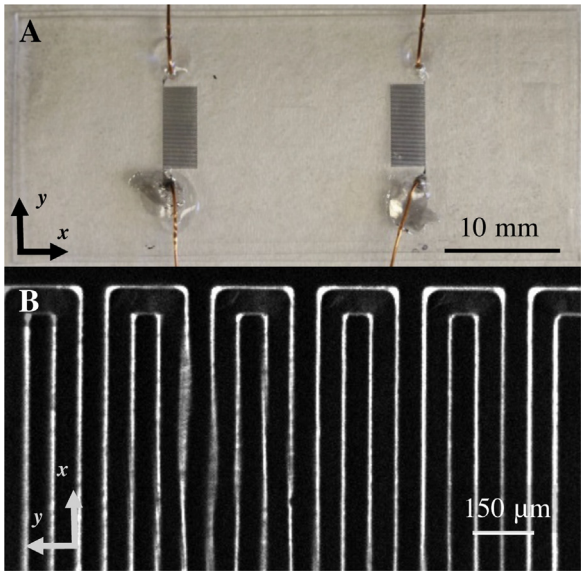


**Fig. 2.** Resistive liquid metal strain gauges embedded in artificial skin. (A) An assembled shear sensor skin shows a pair of eGaIn microfluidic channels embedded in PDMS. (B) Microscopic view of the serpentine microchannel adjacent to a reservoir.

The interface between the PDMS film and acrylic half-round was lubricated by gear oil (SHC 627, Mobil, Irving, TX, USA). A force/torque (F/T) transducer (Nano 17, ATI, Apex, NC) was mounted above the sensor to provide an independent measure of the forces applied to the sensor skin. The force transducer was attached to a loading tip that consisted of a 14 mm diameter cylindrical acrylic plate. The stage supporting the sensor skin was manually actuated to displace the sensorized fingertip relative to the force loading tip. Normal and shear force profiles were simultaneously measured by the sensor skin and force transducer.

Fig. 3B shows the external electrical equipment. The two sensor strain gauges were connected in series with a sourcemeter (6430, Keithley, Cleveland, OH, USA) applying 5 mA DC current. We measured the voltage across each strain gauge using a low frequency data acquisition card (Personal Daq/55, Measurement Computing, Norton, MA) at 10 Hz. The resistance of each strain gauge is determined $R_{2,0}$using Ohm's law. The resistances at zero load are recorded as $R_{1,0}$ and

The normalized sensor response during experiments are calculated using Eq. (1) as a function of strain gauge resistance changes, $\Delta R_1$ and $\Delta R_2$. A circuit diagram is provided in the supplemental information Section 5. According to a simple convection analysis, Joule heating should not result in an increase of device temperature of more than 5 °C.

We applied normal force by moving the stage vertically and then stepwise increased shear forces (0.1 N increments) by moving the stage horizontally. Each data point was averaged over 1 s.

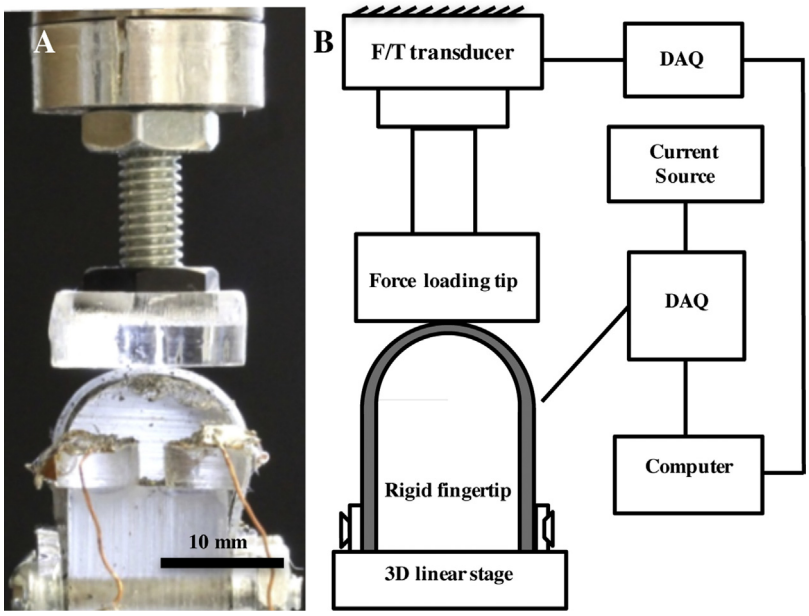


**Fig. 3.** Experimental setup for sensor characterization under controlled normal and shear forces. (A) The artificial skin is mounted on an acrylic half round and the two mounting brackets are fastened by a bolt and nut. The acrylic loading tip is rigidly connected to the F/T transducer on the top. (B) Schematic of the mechanical and electrical aspects of the experimental setup. Artificial skin is shown as the grey area. The shear sensing skin is mounted on a rigid fingertip that can be displaced in 3D to generate normal and shear forces. The two sensor skin strain gauges are connected in series with a current source of 5 mA. Voltages across each strain gauge are measured by data acquisition equipment.

The resistances without load ($R_{1,0}$ and $R_{2,0}$) were measured before each loading scenario for normalization during that loading scenario using Eq. (1).

## 4. Results and discussion

In this section, we present an analytical analysis of the shear sensor skin response and computational predictions of the sensor deformation under various normal and shear forces. The static calibration of the shear force sensor is presented and critical performance criteria are calculated including sensitivity, shear force resolution, and prediction interval.

### 4.1. Analytical analysis

The shear sensor skin response can be estimated using a simple analytical model with a few assumptions. Here we consider the skin with uniform cross section, negligible friction with underlying finger core, uniform strain distribution across $z$-direction as indicated in Fig. 1. We also assume that internal forces in the tension region alone is in balance with the external shear force, since the compression region is buckling and the strain magnitude is negligible in comparison to that of the tension region. The circumferential strain $\varepsilon$ at the location of the strain gauge can be simply represented as $\varepsilon = F_t/EA$, where $F_t$ is the applied shear force at the fingerpad, $E$ is Young's modulus of the PDMS, $A$ is the cross sectional area. The normalized sensor response is $\varepsilon F$, where $F$ is the gauge factor. The sensitivity is the normalized sensor response per unit shear force given as $F/EA$. This estimate results in a sensitivity of 0.088 $N^{-1}$, which we will show compares well with the measured and computationally predicted values presented in Table 1. This analytical analysis shows that the sensor sensitivity is a linear function of the material stiffness and cross-sectional thickness. As long as the condition of negligible friction forces between the skin and the effector are maintained, the fingertip geometry should not have an effect on the sensitivity. A softer skin material and smaller cross section area results in higher sensitivity, yet the softer, thinner skin may be more susceptible to failure at high shear forces and is likely to show significant non-linear response at higher shear forces due to strain softening. Design tradeoff between range, sensitivity, and linearity can be estimated using this simplified analytical model.

**Table 1**
Sensitivity of the shear force sensor as calculated from computational models and experimental characterizations under different normal forces. Experimental sensitivity was calculated from a linear regression of shear force magnitude under 1.2 N.

| Normal force [N] | Sensitivity [$N^{-1}$] | |
|---|---|---|
| | Computation | Experiment |
| 0.5 | 0.078 | 0.078 |
| 1.0 | 0.078 | 0.076 |
| 1.5 | 0.078 | 0.080 |
| 2.0 | 0.078 | 0.080 |
| Average | 0.078 | 0.078 |

### 4.2. Shear sensor simulations

Fig. 4 shows simulation strain distribution contours with a 1 N normal force and shear forces of 0.5 and 1 N in subfigures A and B, respectively. In each case, the normal force was applied first and then the shear force was increased from zero in increments of 0.1 N. In both cases, a circumferential tensile strain develops on the tail-side of the shear force vector (-$x$ direction in Fig. 4) while a circumferential compressive strain develops on the head-side of the shear force vector (+$x$ direction in Fig. 4). The magnitude of tensile strain is larger than that of compressive strain due to buckling of the compressed region of the sensor skin. The stretching and compression of the sensor skin is asymmetric, resulting in an overall increase in skin length that results in a separation of the sensor from the rigid core, that is analogous to a bulging finger pad under significant shear stress. A large magnitude tensile strain forms at the location that the normal force is applied (0,−6.35) due to Poisson's effect.

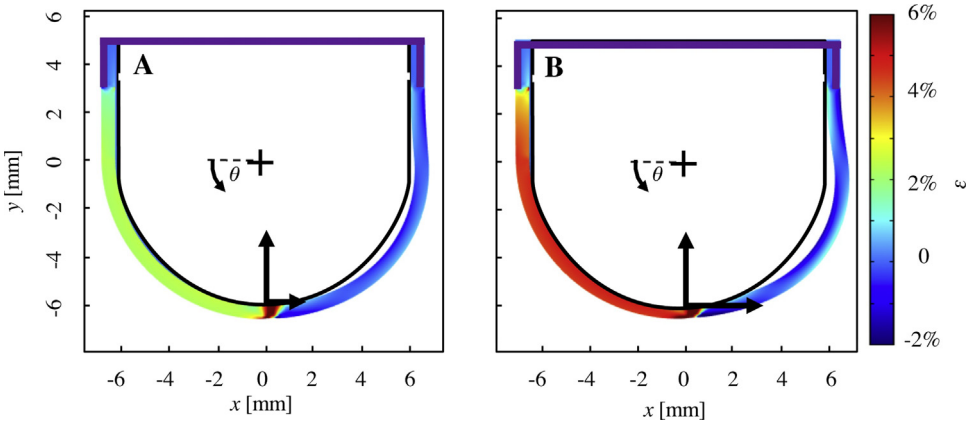


**Fig. 4.** Circumferential strain distribution contour with normal force $F_n$ and shear forces $F_t$. (A) and (B) show skin strain for $F_n$ = 1.0 N with $F_t$ = 0.5 N and $F_t$ = 1.0 N, respectively. The external force, whose normal and tangential components are shown as bold arrows, is applied at the bottom center of the sensor skin at (0,−6.35). The color legend shows the circumferential strain scale with positive and negative values corresponding to tensile and compressive strain, respectively. The purple lines show the fixed boundaries. The shear sensing skin is divided into regions of circumferential tensile and compressive strain, with compression and buckling occurring on the side of the finger to which the shear force vector head points. The magnitude of tensile strain is significantly higher than compressive strain, and is a strong function of shear force. (For interpretation of the references to colour in this figure legend, the reader is referred to the web version of this article.)

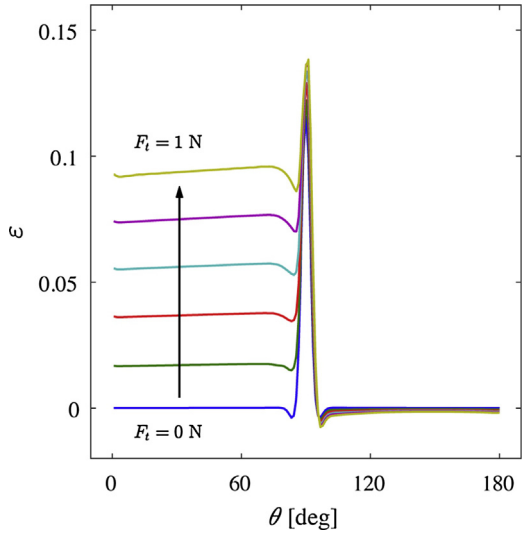


**Fig. 5.** Circumferential strain at the midline of skin thickness with respect to angular position with a normal force of 1 N. The origin of the cylindrical coordinate system is (0,0) in Fig. 4, where $\theta = 90^\circ$ is the location where the external force is applied (0,−6). In this example, the compressive side is where $\theta > 90^\circ$ and the tensile side is $\theta < 90^\circ$. The applied tangential force magnitude increases from $F_t$ = 0 (bottom blue line) to $F_t$ = 1 N with 0.1 N increments along the direction of the arrow. (For interpretation of the references to colour in this figure legend, the reader is referred to the web version of this article.)

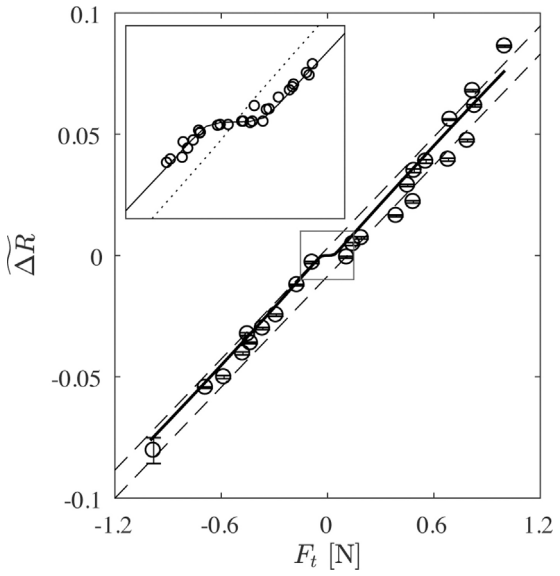


**Fig. 6.** Experimental (circles) and computational (solid line) normalized resistance sensor response as a function of the applied shear force. The applied normal force is 1 N and the range of the shear force is ±1 N. The dashed grey lines show the experimental data prediction interval at a 95% confidence level. The 95% confidence interval of each data point is presented using error bars, but is too small to discern because it is smaller than the marker. The inset shows a magnified view of the experimental and computational normalized resistance sensor response with respect to shear force in the range of ±0.15 N. The grey dotted line shows the simulated prediction of a zero-friction device. It can be inferred that the sensor performance for small shear forces could be improved by reducing the friction between the shear sensor skin and the fingertip.

Fig. 5 shows the circumferential strain, $\varepsilon_{\theta\theta}$, as a function of angular position at a normal force of 1 N and shear force ranging from 0 to 1 N. When there is only a normal force, the circumferential strain is nonzero only at the point of contact ($\theta = 90$)due to the Poisson's effect. When a shear force is applied, relatively constant tensile and compressive strains develop on the tail- ($\theta < 90^\circ$) and head-side ($\theta > 90^\circ$) on the respective sides of the shear force vector. The circumferential strain is near zero on the compressive side $\theta > 90$. Circumferential strain in the tensile region ($\theta < 90^\circ$)is a strong function of shear force yet a weak function of angular position ( < 4%). According to the classical belt friction problem, the circumferential strain should decrease from the point of contact to the proximity of the fixed boundary due to friction; however, with the static friction coefficient of 0.04, there is no significant variation with position. This suggests that the sensors could be positioned anywhere along the sensor skin, without sacrificing sensitivity, as long as they are sufficiently far from the point of contact with physical objects where they might be influenced by Poisson's effect. Placing the sensors near the nail bed reduces the probability of the sensors being subjected to interference from normal forces and makes room for other sensor modalities, such as normal force or temperature, that might benefit from close proximity to the point of contact.

Fig. 6 shows the predicted normalized sensor response, $\widetilde{\Delta R}$, as a function of the applied shear force for 1 N of normal force. The simulations show that the sensor response is linear with applied shear force over most of the small shear forces examined here. The inset of Fig. 6 shows the predicted normalized sensor response as a function of the applied shear force over a smaller range of shear

forces (<0.15 N) to elucidate the sensor deadband due to the friction between the sensor skin and the rigid core. The sensor response remains at zero before the shear force overcomes the static friction force and the skin is free to slip against the rigid core, thus the deadband region increases with the normal force. At moderate normal forces of 1 N and friction coefficient as 0.04, we predict the minimum shear force measurement to be 0.04 N.

The slope of normalized sensor response with respect to the applied shear force throughout the working range is defined as the sensitivity. Table 1 shows that the predicted sensitivity for several applied normal forces ranging from 0.5 N to 2 N is 7.8 %/N. The predicted sensitivity does not change with the applied normal force, suggesting that the response of the shear sensor, in the light touch regime, is independent of the applied normal force. This is advantageous because the shear force can be resolved without knowledge of the normal force.

### 4.3. Sensor static characterization

In this section, we present experimental results from static loading experiments. Fig. 6 shows measurements of the normalized sensor response as a function of the shear force with a 1 N normal force. The measurements agree well with the predicted response with average deviations less than 8%. Due to buckling behavior on the compressive side, the strain gauge response magnitude from the compressive side is much lower than that from the tension side. This behavior is observed in both numerical simulations and experimental results where individual strain gauge responses are in good agreement. Details are presented in the supplemental information in Section 8. The sensor's response is repeatable with repetitive shear force up to 5 N and starts to respond at 0.04 N as predicted, with 1 N applied normal force due to static friction. The simulations show that the minimum shear force is required to overcome static friction and exhibit a linear response to applied shear force depending on the friction coefficient and applied normal force. We define the noise floor as the standard deviation of the normalized sensor response over a 1 s measurement interval at a constant shear force value. Using this definition, the average noise floor is 1.6 mN, which results in a dynamic range (with a maximum of 5 N) of more than 10-bits. [6,13]

We subject the sensor to various normal forces with no applied shear force, which should not result in any measured shear force if the sensor is properly decoupled, and show that the sensor reports a normalized sensor response of less than 1.24E-4 (or 1.45 mN), which is less than the noise floor. The shear force sensor is insensitive to shear force in the transverse direction as shown in Fig. S8 in the supplement. The drift of the sensor is evaluated by the standard deviation of the sensor response to a constant shear force load over time. The sensor was loaded with $F_n = 0.5$ N and $F_t = 0.15$N for 1 h and data were collected at 0.01 Hz. The standard deviation of the normalized sensor response is 1.48E-4 (or 1.73 mN). The precision of the shear sensor skin is characterized by a prediction interval that was calculated to be ±0.0802 N at 95% confidence. Details of the mathematical representation of the prediction interval are presented in the supplemental information.

Fig. 7 shows the normalized sensor response as a function of the shear force for different applied normal forces. This experiment is conducted over a larger range of shear forces (±1.6 N) than is shown in Fig. 6 and exhibits a nonlinear response at higher shear forces. At shear forces greater than 1.2 N, the slope of the data increases, resulting an increase in the sensor sensitivity. Linear regression over this entire range of applied shear forces results in an error less than 30% at high shear force levels. For simplicity, we use simple linear fits to determine the sensitivity for shear force magnitude less than 1.2 N, provided in Table 1. These values agree well with the model predictions within 5%. If desired, a nonlinear fit can be implemented to better represent the sensor response at high shear force levels, as shown in the supplemental information.

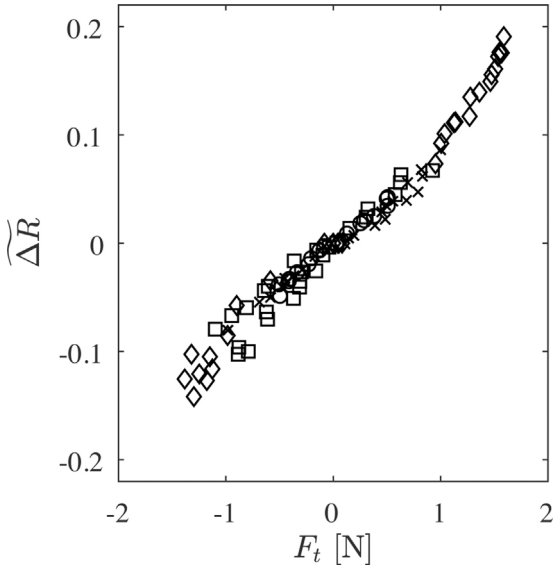


**Fig. 7.** Experimental normalized sensor response as a function of shear force at normal force levels of $F_n = 0.5$ N (Δ), $F_n = 1$ N (□), $F_n = 1.5$ N (○), and $F_n = 2$ N (◊). Data points for small shear forces between −0.5 N and 0.5 N at various normal forces overlap and some are not shown to increase plot clarity. The normalized sensor response is linear at small shear force (magnitude less than 1.2 N) and exhibits increasing sensitivity at higher shear forces. The sensitivity, visualized as the slope of the data, is relatively uniform across the range of normal forces examined. The deviation from a linear calibration at larger shear forces may be the result of local high strains generated from non-uniform loading in the *z* direction (as defined in Fig. 1).

We suggest that the nonlinearity observed at higher shear forces is due to the nonlinear mechanical properties of PDMS at high strain as well as the stress variation in the out-of-plane dimension (z-direction) becoming non-negligible for larger shear forces. The reduction of PDMS stiffness at high strain partially explains the increase in measured sensitivity at high shear forces. As stated in the supplemental information, PDMS starts to soften at approximately 9% strain, and its deviation from linear elasticity can be as much as 14% at 20% strain. In addition, our two-dimensional simulation assumed a line load at the center of the fingerpad (considering a 2D simulation is infinite in the third (*z*) dimension), whereas in the experiments only part of the skin in the *z*-direction (as defined in Fig. 1) is loaded. Local high strain occurred in the *y* dimension that the simulation did not take into consideration. This nonlinearity observed in experiments may be captured in the simulations using a more comprehensive, three-dimensional, hyperelastic mechanical finite element model.

The above experiments are all performed at room temperature of around 25 °C. In order to evaluate the sensors sensitivity to temperature, we calibrated the sensor under $F_n = 1$ N at elevated temperature of 40 °C. The skin was heated with a heat gun and the temperature was verified by a thermocouple mounted adjacent to the shear sensor skin. Fig. 8 shows normalized sensor response as a function of shear force at 25 °C and 40 °C. The sensor response overlaps and no change of sensitivity can be observed above the data variation. Linear regression showed less than 2% of sensitivity change. The sensor response suggests that the sensitivity is likely a weak function of temperature and the calibration does not change within the investigated temperature range. The change of resistivity of eGaIn for the 15 °C temperature raise is approximately 1.1% [55]. The apparent strain induced by thermal expansion is governed by PDMS instead of eGaIn because relatively large reservoirs on the ends of the channels could accommodate any excessive liquid

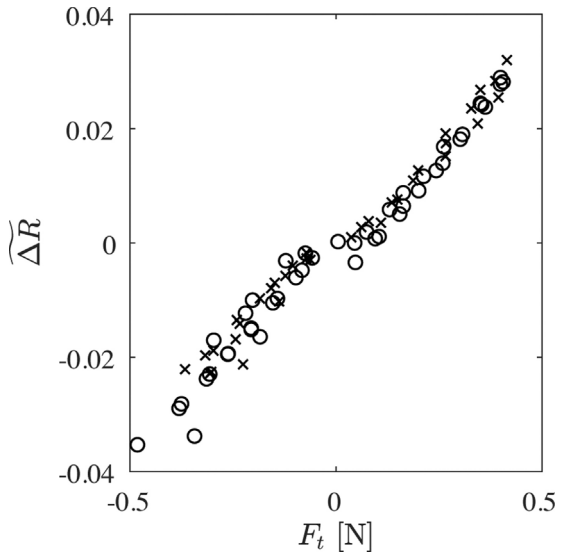


**Fig. 8.** Experimental normalized sensor responses as a function of shear force at $F_n$ = 1 N under room, 25 °C, (circles) and elevated, 40 °C, temperature (crosses). Data markers overlap and change in the sensitivity is not observed.

metal. Linear thermal expansion coefficient of PDMS is 3.2E-4 °C$^{-1}$ [56], therefore the apparent strain for the 15 °C temperature raise is less than 0.5%. Such variances induced by temperature changes are significantly less than the uncertainty observed in the experiments.

## 5. Summary

Here we report a bioinspired, thin and flexible shear force sensor skin that deforms in response to applied shear forces similar to a human fingertip. The shear sensor skin's novelty is that the tension and compression are measured by embedded liquid metal strain gauges that are strategically placed adjacent to the nail bed, away from the point of finger-object contact. This design has the advantage over existing skin based shear sensor designs that it is free from confounding effects of normal forces where the effector and object make contact. This design also provides space for normal force sensors on the palmar aspects of the fingertip, where contact with objects is likely to occur. The resistive shear sensing skin is flexible, conformable to curved surfaces, robust, and insensitive to temperature changes. This shear sensing skin design may be compatible with a range of artificial fingertip geometries when appropriately calibrated to address variations in finger surface geometry as well as friction between the sensor skin and the end effector.

Static finite element models and experiments, in the light touch regime, show matching linear sensor response that is independent of the applied normal force that is validated by a one-dimension analytical analysis,. Precision and dynamic range are useful yet less discussed metrics of force sensor performance and we present statistical analysis to determine these quantities. The shear force sensor has a precision of 0.08 N and exhibits a dynamic range greater than 10-bits (up to 5 N). Such precision is approaching the robotic community's desired sensitivity of 0.01 N [6,13]. Our analytical model shows that the dynamic range of the shear force sensor can be increased by increasing the channel resistance (e.g. by reducing the channel cross section area or increasing the total length). At higher shear forces, the experiments show a nonlinear response where the sensor sensitivity increases at higher shear forces.

Our future work focuses on the development of an integrated sensor skin capable of measuring two dimensions of shear force and normal forces as well as dynamic sensor characterization during end effector interactions with objects and the measurement of vibration.

## Acknowledgments

This material is based upon work supported by the National Science Foundation under Grant No. CBET-1264046 and CBET-1461630. The authors would also like to thank UW NNIN Nanofabrication Facility for training and support in the clean room and Dr. Per G. Reinhall who provided suggestions on the contact mechanics modelling and selection of lubricants. We are grateful to Stefan Foulstone for assistance in generating Fig. 1.

## Appendix A. Supplementary data

Supplementary data associated with this article can be found, in the online version, at http://dx.doi.org/10.1016/j.sna.2017.08.001.

## Reference:

[1] A.W. Goodwin, H.E. Wheat, Sensory signals in neural populations underlying tactile perception and manipulation, Annu. Rev. Neurosci. 27 (1) (2004) 53–77.
[2] J. Monzée, Y. Lamarre, A.M. Smith, The effects of digital anesthesia on force control using a precision grip, J. Neurophysiol. 89 (2) (2003) 672–683.
[3] R.S. Dahiya, G. Metta, M. Valle, G. Sandini, Tactile sensing—from humans to humanoids, Robot. IEEE Trans. On 26 (1) (2010) 1–20.
[4] R.D. Ponce Wong, R.B. Hellman, V.J. Santos, Haptic exploration of fingertip-sized geometric features using a multimodal tactile sensor, Baltimore, MD, May 8, in: Proc SPIE Defense, Security and Sensing/Sensing Technology and Applications "Sensors for Next-Generation Robotics" Conference, vol. 9116, 2014, pp. 911605–1–911605–15.
[5]. M.E.H. Eltaib, J.R. Hewit, Tactile sensing technology for minimal access surgery––a review, Mechatronics 13 (10) (2003) 1163–1177.
[6] M.I. Tiwana, S.J. Redmond, N.H. Lovell, A review of tactile sensing technologies with applications in biomedical engineering, Sens. Actuators Phys. 179 (2012) 17–31.
[7] A.M. Okamura, Haptic feedback in robot-Assisted minimally invasive surgery, Curr. Opin. Urol. 19 (1) (2009) 102–107.
[8] B. Preising, T.C. Hsia, B. Mittelstadt, A literature review: robots in medicine, IEEE Eng. Med. Biol. Mag. 10 (2) (1991) 13–22.
[9] Z. Su, et al., Force estimation and slip detection/classification for grip control using a biomimetic tactile sensor, 2015 IEEE-RAS 15th International Conference on Humanoid Robots (Humanoids) (2015), pp. 297–303.
[10] S. Chitta, J. Sturm, M. Piccoli, W. Burgard, Tactile sensing for mobile manipulation, IEEE Trans. Robot. 27 (3) (2011) 558–568.
[11] M. Weigel, T. Lu, G. Bailly, A. Oulasvirta, C. Majidi, J. Steimle, ISkin: flexible, stretchable and visually customizable on-Body touch sensors for mobile computing, in: Proceedings of the 33rd Annual ACM Conference on Human Factors in Computing Systems, New York, NY, USA, 2015, pp. 2991–3000.
[12] R.S. Johansson, J.R. Flanagan, Tactile sensory control of object manipulation in humans, in: R.H. Masland, T.D. Albright, T.D. Albright, R.H. Masland, P. Dallos, D. Oertel, S. Firestein, G.K. Beauchamp, M.C. Bushnell, A.I. Basbaum, J.H. Kaas, E.P. Gardner (Eds.), The Senses: A Comprehensive Reference, Academic Press, New York, 2008, pp. 67–86.
[13] H. Yousef, M. Boukallel, K. Althoefer, Tactile sensing for dexterous in-hand manipulation in robotics—a review, Sens. Actuators Phys. 167 (2) (2011) 171–187.
[14] Johan Tegin, Jan Wikander, Tactile sensing in intelligent robotic manipulation –a review, Ind. Robot Int. J. 1 (2005) 64–70.
[15] J. Dargahi, S. Najarian, Human tactile perception as a standard for artificial tactile sensing—a review, Int. J. Med. Robot. 1 (1) (2004) 23–35.
[16] K.-U. Kyung, M. Ahn, D.-S. Kwon, M.A. Srinivasan, Perceptual and biomechanical frequency response of human skin: implication for design of tactile displays, Eurohaptics Conference, 2005 and Symposium on Haptic Interfaces for Virtual Environment and Teleoperator Systems, 2005. World Haptics 2005. First Joint (2005), pp. 96–101.
[17] S.P. Patarinski, R.G. Botev, Robot force control: a review, Mechatronics 3 (4) (Aug. 1993) 377–398.
[18] J.A. Fishel, G.E. Loeb, Bayesian exploration for intelligent identification of textures, Front. Neurorob. 6 (2012).
[19] M.R. Tremblay, M.R. Cutkosky, Estimating friction using incipient slip sensing during a manipulation task, IEEE International Conference on Robotics and Automation, 1993. Proceedings 1 (1993), pp. 429–434.
[20] R. Howe, M. Cutkosky, Sensing skin acceleration for slip and texture perception, IEEE International Conference on Robotics and Automation, 1989. Proceedings 1 (1989), pp. 145–150.
[21] H. Zhao, K. O'Brien, S. Li, R.F. Shepherd, Optoelectronically innervated soft prosthetic hand via stretchable optical waveguides, Sci. Robot. 1 (1) (2016) eaai7529.

[22] N. Wettels, V.J. Santos, R.S. Johansson, G.E. Loeb, Biomimetic tactile sensor array, Adv. Robot. 22 (8) (2008) 829–849.
[23] R.D. Ponce Wong, J.D. Posner, V.J. Santos, Flexible microfluidic normal force sensor skin for tactile feedback, Sens. Actuators Phys. 179 (2012) 62–69.
[24] M.L. Hammock, A. Chortos, B.C.-K. Tee, J.B.-H. Tok, Z. Bao, 25th anniversary article: the evolution of electronic skin (E-Skin): a brief history, design considerations, and recent progress, Adv. Mater. 25 (42) (2013) 5997–6038.
[25] F.L. Hammond, R.K. Kramer, Q. Wan, R.D. Howe, R.J. Wood, Soft tactile sensor arrays for force feedback in micromanipulation, IEEE Sens. J. 14 (5) (2014) 1443–1452.
[26] F.L. Hammond, Y. Menguc, R.J. Wood, Toward a modular soft sensor-embedded glove for human hand motion and tactile pressure measurement, Intelligent Robots and Systems (IROS 2014), 2014 IEEE/RSJ International Conference (2014), pp. 4000–4007.
[27] E.S. Hwang, J. h Seo, Y.J. Kim, A polymer-Based flexible tactile sensor for both normal and shear load detections and its application for robotics, J. Microelectromech. Syst. 16 (3) (2007) 556–563.
[28] L. Viry, et al., Flexible three-Axial force sensor for soft and highly sensitive artificial touch, Adv. Mater. 17 (2014) 2659–2664.
[29] B. Zhu, et al., Microstructured graphene arrays for highly sensitive flexible tactile sensors, Small 18 (2014) 3625–3631.
[30] J. Engel, J. Chen, N. Chen, S. Pandya, C. Liu, Multi-walled carbon nanotube filled conductive elastomers: materials and application to micro transducers, 19th IEEE International Conference on Micro Electro Mechanical Systems (2006), pp. 246–249.
[31] M. Sohgawa, et al., Tactile array sensor with inclined chromium/silicon piezoresistive cantilevers embedded in elastomer, TRANSDUCERS 2009-2009 International Solid-State Sensors, Actuators and Microsystems Conference (2009), pp. 284–287.
[32] Y.-J. Yang, et al., An integrated flexible temperature and tactile sensing array using PI-copper films, Sens. Actuators Phys. 143 (1) (2008) 143–153.
[33] P. Peng, R. Rajamani, A.G. Erdman, Flexible tactile sensor for tissue elasticity measurements, J. Microelectromech. Syst. 18 (6) (2009) 1226–1233.
[34] H.K. Lee, S.I. Chang, E. Yoon, A flexible polymer tactile sensor: fabrication and modular expandability for large area deployment, J. Microelectromech. Syst. 15 (6) (2006) 1681–1686.
[35] A. Drimus, G. Kootstra, A. Bilberg, D. Kragic, Design of a flexible tactile sensor for classification of rigid and deformable objects, Robot. Auton. Syst. 62 (1) (2014) 3–15.
[36] A. Charalambides, S. Bergbreiter, A novel all-elastomer MEMS tactile sensor for high dynamic range shear and normal force sensing, J. Micromech. Microeng. 25 (9) (2015) 095009.
[37] F. Schneider, T. Fellner, J. Wilde, U. Wallrabe, Mechanical properties of silicones for MEMS, J. Micromech. Microeng. 18 (6) (2008) 065008.
[38] F.L. Hammond, R.K. Kramer, Q. Wan, R.D. Howe, R.J. Wood, Soft tactile sensor arrays for micromanipulation, 2012 IEEE/RSJ International Conference on Intelligent Robots and Systems (IROS) (2012), pp. 25–32.
[39] Y.-L. Park, C. Majidi, R. Kramer, P. Bérard, R.J. Wood, Hyperelastic pressure sensing with a liquid-embedded elastomer, J. Micromech. Microeng. 20 (12) (2010) 125029.
[40] M.D. Dickey, R.C. Chiechi, R.J. Larsen, E.A. Weiss, D.A. Weitz, G.M. Whitesides, Eutectic gallium-Indium (EGaIn): a liquid metal alloy for the formation of stable structures in microchannels at room temperature, Adv. Funct. Mater. 18 (7) (2008) 1097–1104.
[41] G.J. Hayes, J.H. So, A. Qusba, M.D. Dickey, G. Lazzi, Flexible liquid metal alloy (EGaIn) microstrip patch antenna, IEEE Trans. Antennas Propag. 60 (5) (2012) 2151–2156.
[42] I.D. Johnston, D.K. McCluskey, C.K.L. Tan, M.C. Tracey, Mechanical characterization of bulk Sylgard 184 for microfluidics and microengineering, J. Micromech. Microeng. 24 (3) (2014) 035017.
[43] M.W. Keller, S.R. White, N.R. Sottos, Torsion fatigue response of self-healing poly(dimethylsiloxane) elastomers, Polymer 49 (13–14) (2008) 3136–3145.
[44] P. Roberts, D.D. Damian, W. Shan, T. Lu, C. Majidi, Soft-matter capacitive sensor for measuring shear and pressure deformation, 2013 IEEE International Conference on Robotics and Automation (ICRA) (2013), pp. 3529–3534.
[45] D.M. Vogt, Y.-L. Park, R.J. Wood, Design and characterization of a soft multi-axis force sensor using embedded microfluidic channels, IEEE Sens. J. 13 (10) (2013) 4056–4064.
[46] C. Majidi, R. Kramer, R.J. Wood, A non-differential elastomer curvature sensor for softer-than-skin electronics, Smart Mater. Struct. 20 (10) (2011) 105017.
[47] Y.-L. Park, B.-R. Chen, R.J. Wood, Design and fabrication of soft artificial skin using embedded microchannels and liquid conductors, IEEE Sens. J. 12 (8) (2012) 2711–2718.
[48] K. Doudrick, et al., Different shades of oxide: from nanoscale wetting mechanisms to contact printing of gallium-based liquid metals, Langmuir 30 (23) (2014) 6867–6877.
[49] C. Ladd, J.-H. So, J. Muth, M.D. Dickey, 3D printing of free standing liquid metal microstructures, Adv. Mater. 25 (36) (2013) 5081–5085.
[50] L. Wang, J. Liu, Liquid Metal Inks for Flexible Electronics and 3D Printing: A Review, in: ASME 2014 International Mechanical Engineering Congress and Exposition, American Society of Mechanical Engineers, 2014.
[51] J. Wissman, T. Lu, C. Majidi, Soft-matter electronics with stencil lithography, in: SENSORS, 2013 IEEE, IEEE, 2013, pp. 1–4.
[52] V.N. Parthasarathy, C.M. Graichen, A.F. Hathaway, A comparison of tetrahedron quality measures, Finite Elem. Anal. Des. 3 (1994) 255–261.
[53] M. Meyer, R.M. Kirby, R. Whitaker, Topology accuracy, and quality of isosurface meshes using dynamic particles, IEEE Trans. Vis. Comput. Graph. 13 (6) (2007) 1704–1711.
[54] J. Shewchuk, What Is a Good Linear Finite Element? Interpolation, Conditioning, Anisotropy, and Quality Measures (preprint), 3, University of California at Berkeley, 2002.
[55]. S. Yu, M. Kaviany, Electrical, thermal, and species transport properties of liquid eutectic Ga-In and Ga-In-Sn from first principles, J. Chem. Phys. 140 (6) (2014) 064303.
[56] B.E. Schubert, D. Floreano, Variable stiffness material based on rigid low-melting-point-alloy microstructures embedded in soft poly(dimethylsiloxane) (PDMS), RSC Adv. 3 (46) (2013) 24671–24679.

## Biographies

**Jianzhu Yin** obtained his B.Eng. degree in Thermal Engineering at Tsinghua University in June 2012. He is currently in the Mechanical Engineering Ph.D. program at University of Washington. His work focuses on the design, fabrication, characterization, and application integration of microfluidic tactile sensors.

**Veronica J. Santos** is an Associate Professor in the Mechanical and Aerospace Engineering Department at the University of California, Los Angeles, and Director of the UCLA Biomechatronics Lab. Dr. Santos earned her Ph.D. in mechanical engineering with a biometry minor from Cornell University (2007). While a postdoc at the University of Southern California, she contributed to the development of a biomimetic tactile sensor for prosthetic hands. Her research interests include human hand biomechanics, human-machine systems, haptics, tactile sensors, machine perception, prosthetics, and robotics for grasp and manipulation. She currently serves on the Editorial Boards for the ASME Journal of Mechanisms and Robotics and the IEEE International Conference on Robotics and Automation.

**Jonathan D. Posner** is an associate professor joint in Mechanical Engineering and Chemical Engineering departments as well as adjunct professor in Family Medicine at University of Washington. He directs UW's Engineering Innovation in Health program that focuses on developing technical solutions to pressing challenges in health and healthcare. Dr. Posner earned his Ph.D. (2001) degree in Mechanical Engineering at the UC Irvine, was a postdoctoral fellow at the Stanford University, and spent 18 months at the von Karman Institute for Fluid Mechanics. Jonathan's group works on diverse set of need-driven research projects including medical devices, point-of-care biochemical diagnostics, improved cookstoves for the developing world, and helmets that reduce the risk of concussion.